Terahertz emission from $YBa_2Cu_3O_{7-\delta}$ thin films via bulk electric-quadrupole–magnetic-dipole optical rectification

Jennifer L. W. Siders, S. A. Trugman, F. H. Garzon, R. J. Houlton, and A. J. Taylor*
Materials Science and Technology Division and Theoretical Division, Los Alamos National Laboratory, MS K764, Los Alamos, New Mexico 87545
(Received 1 December 1999)

We report the observation of terahertz emission from $YBa_2Cu_3O_{7-\delta}$ thin films excited by 1.5-eV, 150-fs pulses in the absence of external electric or magnetic fields. This emission is characterized for optimally doped $\delta=0$ films and underdoped $\delta=0.5$ films, over a range of temperatures T, $4\,K<T<300\,K$, where the films change from superconductors to correlated metals. It exhibits a pronounced 4ϕ dependence with respect to the azimuthal angle ϕ. We demonstrate that this emission is generated by optical rectification due to the bulk electric quadrupole and magnetic dipole source terms. A model of this emission, assuming that the nonlinearity results from transport of carriers with different masses and relaxation times in the three crystallographic directions, is consistent with the data. A fit of the data to this model yields values for the anisotropic masses and relaxation times in $YBa_2Cu_3O_{7-\delta}$ thin films.

I. INTRODUCTION

The generation of subpicosecond terahertz (THz) bandwidth radiation via the illumination of nonlinear materials with visible femtosecond pulses is of interest both as a spectroscopic source and as a probe of the electronic and vibrational properties of materials.[1–4] Such THz emission studies are based on coherent optical excitation of a material and the subsequent temporal evolution of the far-infrared dipole associated with the excitation. THz emission has previously been observed from superconducting ($T<T_C$) $YBa_2Cu_3O_7$ thin films configured as biased antennas[5] and unbiased in a magnetic field.[6] Here we describe the observation of THz emission from $YBa_2Cu_3O_{7-\delta}$ (YBCO) thin films in the absence of an external electric or magnetic field. This THz emission is generated by optical rectification due to the bulk electric quadrupole and magnetic dipole source terms, and to our knowledge comprises the first observation of such source terms in THz emission. A model of this emission, assuming that the nonlinearity results from transport of carriers with different masses and relaxation times in the three crystallographic directions, is presented and the data are analyzed using this model.

II. EXPERIMENT

We use *c*-axis-oriented, twinned $YBa_2Cu_3O_{7-\delta}$ films deposited on 1-mm-thick (100) MgO substrates using dc off-axis sputtering. X-ray analysis of the films indicates that the *c* axis of the film is well aligned with the surface normal, and that the *a* and *b* axes are aligned with the MgO axes. Two optimally doped $\delta=0$ films with thicknesses of 60 and 300 nm are studied. The superconducting transition temperature for these films is 85 K. The 300-nm-thick underdoped $YBa_2Cu_3O_{6.5}$ film has a transition temperature of 55 K.

The experimental setup for the detection of THz emission is as follows: The 800-nm, 150-fs output of a 1-kHz amplified Ti:sapphire laser system is split into a pump pulse, which is mechanically chopped at 200 Hz and used to excite the sample, and a gate pulse, temporally delayed with respect to the pump, which drives a photoconductive THz detector. The THz emission transmitted through the sample is collected with a pair of gold-coated parabolic mirrors and focused onto a photoconductive detector consisting of 2.5-mm-gap electrodes deposited on radiation-damaged silicon-on-sapphire. The resultant temporal resolution is about 1 ps. The emitted THz waveform is measured by scanning the gate delay relative to the pump and synchronously detecting the output of the photoconductive detector at the pump chopping frequency. A wire grid polarizer placed between the sample and the detector is used to select either *P*- or *S*-polarized THz radiation.

III. ROOM-TEMPERATURE RESULTS

The amplitude of the emitted THz waveforms exhibits a nontrivial dependence on the doping level of the sample the polarization of the detected and emitted radiation, as well as on the angle of incidence θ of the optical excitation and the azimuthal orientation ϕ of the crystal with respect to the twinned *a* and *b* axes. However, the waveforms are always dispersion-shaped with a width limited by the 1-ps detector resolution. Figure 1 reveals the emitted waveforms from a 300-nm-thick $YBa_2Cu_3O_7$ film at $T=300\,K$ excited at $\theta=50°$ and $\phi=22.5°$, for *S*-polarized incident and detected radiation (SS), *S*-polarized incident radiation and *P*-polarized detected radiation (SP), *P*-polarized incident radiation and *S*-polarized detected radiation (PS), and *P*-polarized incident and detected radiation (PP). Such dispersion-shaped waveforms are typically indicative of a nonlinearity due to free rather than bound carriers, where the radiated terahertz field is proportional to the first derivative of the photoinduced current, $\partial J/\partial t$.

The amplitude of the emitted terahertz electric field scales linearly with the incident optical intensity (and therefore quadratically with incident electric field) up to fluences of 6

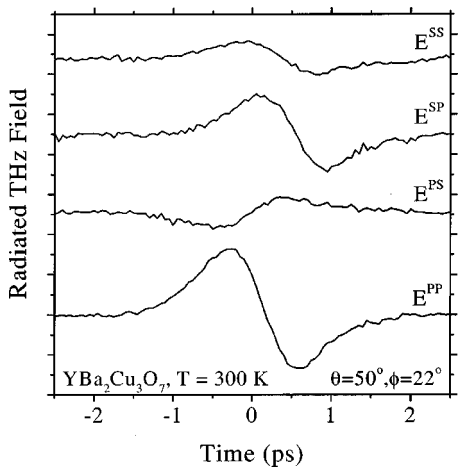

FIG. 1. Emitted THz waveforms (offset vertically) from a 300-nm-thick $YBa_2Cu_3O_7$ film at $T=300$ K excited at $\theta=50°$ and $\phi=22.5°$, for *S S*-polarized incident and detected radiation (SS), *S*-polarized incident radiation and *P*-polarized detected radiation (SP), *P*-polarized incident radiation and *S*-polarized detected radiation (PS), and *P*-polarized incident and detected radiation (PP).

mJ/cm^2, consistent with a second order, nonlinear optical process; however, because YBCO is centrosymmetric, the bulk electric dipole contribution to second order nonlinear susceptibility, χ^2, vanishes. Since different χ^2 processes exhibit distinctive dependences on incident and detected polarizations, as well as on orientation of crystal axes, we measure the peak-to-peak emitted terahertz field as a function of incident and detected polarization and rotation, ϕ, about the surface normal. (For this measurement the waveform for E^{SS} in Fig. 1 has a positive amplitude, while the waveform for E^{PS} has a negative amplitude.) The results for $YBa_2Cu_3O_7$ at $T=300$ K are shown in Fig. 2(a) (points), while the results for $YBa_2Cu_3O_{6.5}$ are shown in Fig. 2(b) (points). For both materials the strong anisotropy with 4ϕ symmetry [$\cos(4\phi)$ for *P*-detected emission and $\sin(4\phi)$ for *S*-detected emission] in the emitted field is consistent with a bulk electric quadrupole/magnetic dipole process from a twinned orthorhombic crystal like $YBa_2Cu_3O_{7-\delta}$. We further note that such a 4ϕ symmetry cannot occur via an electric dipole process even in the presence of a surface field.[7]

Formally, the induced polarization for THz generation via a bulk electric quadrupole/magnetic dipole χ^2 process can be written as[7]

$$P^{(2)}_{q,i}(\Omega)=\chi^{(2)}_{q,ijkl}(\Omega=\omega-\omega)E_j\partial x_k E_l. \qquad (1)$$

For an arbitrary material the fourth-rank tensor $\chi^{(2)}_q$ will have 81 independent elements. For a twinned orthorhombic material, the independent, nonvanishing tensor elements are $\chi^{(2)}_{q,iiii}$, $\chi^{(2)}_{q,iijj}$, $\chi^{(2)}_{q,ijji}$, and $\chi^{(2)}_{q,ijij}$, where the tensor is expressed in terms of the crystallographic axis and *i* and *j* are distinct elements. (Twinning is incorporated into the formalism by allowing the *x* and *y* axes to become interchangeable in the analysis.) The resulting form for THz radiation $E^{\alpha,\beta}$ (where α refers to the input and β refers to the output polarization) due to a bulk electric quadrupole/magnetic dipole process in *c*-axis-oriented, twinned $YBa_2Cu_3O_{7-\delta}$ is presented in Table I. Both the formal analysis in Table I and the data in Fig. 2 exhibit the following features: The *P*-detected

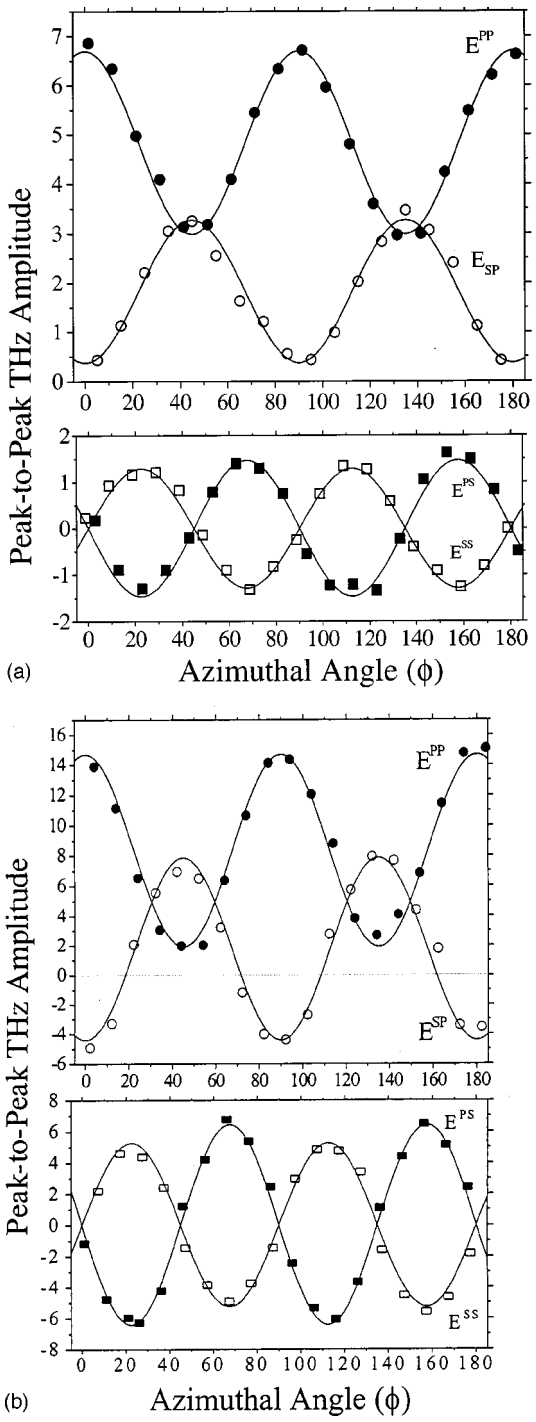

FIG. 2. (a) Peak-to-Peak THz field amplitude vs azimuthal angle ϕ for a $YBa_2Cu_3O_7$ film excited by *P*-(filled symbols) or *S*-polarized (open symbols), 1.5 eV pulses at an incident angle of 50° and detecting *P*-(circles) or *S*-polarized (rectangles) radiation. The uncertainty in ϕ is ±2°, and the uncertainty in the THz field amplitude is ±0.3. The solid curves are fits to the data of the forms $E^{PP}=1.9\{\cos(4\phi)+2.7\}$, $E^{SP}=1.45\{1.3-\cos(4\phi)\}$, $E^{PS}=-1.5\sin(4\phi)$, $E^{SS}=1.3\sin(4\phi)$. (b) Peak-to-peak THz field amplitude vs azimuthal angle for a $YBa_2Cu_3O_{6.5}$ film excited by *P*-(filled symbols) or *S*-polarized (open symbols), 1.5-eV pulses at an incident angle of 50° and detecting *P*-(circles) or *S*-polarized (rectangles) radiation. The uncertainty in ϕ is ±2° and the uncertainty in the THz field amplitude is ±0.6. The solid curves are fits to the data of the forms $E^{PP}=6.4\{\cos(4\phi)+1.3\}$, $E^{SP}=6.1\{0.3-\cos(4\phi)\}$, $E^{PS}=-6.4\sin(4\phi)$, and $E^{SS}=5.3\sin(4\phi)$.

TABLE I. The resulting form for THz radiation $E^{\alpha,\beta}$ (where α refers to the input and β refers to the output polarization) due to a bulk electric quadrupole/magnetic dipole process in *c*-axis-oriented, twinned $YBa_2Cu_3O_{7-\delta}$, where ε_o is a constant proportional to the incident optical intensity, and $\zeta^{(2)}_{q,ij}=\chi^{(2)}_{q,iiii}-\chi^{(2)}_{q,ijji}-\chi^{(2)}_{q,iijj}-\chi^{(2)}_{q,ijij}$.

$E^{SS}=\varepsilon_o \sin\theta'(\zeta^{(2)}_{q,xy}+\zeta^{(2)}_{q,yx})\sin(4\phi)$
$E^{PS}=-\varepsilon_o \sin\theta' \cos^2\theta'(\zeta^{(2)}_{q,xy}+\zeta^{(2)}_{q,yx})\sin(4\phi)$
$E^{SP}=\varepsilon_o \sin\theta' \cos\theta'\{(\zeta^{(2)}_{q,xy}+\zeta^{(2)}_{q,yx})[1-\cos(4\phi)]$ $+4(\chi^{(2)}_{q,xyxy}+\chi^{(2)}_{q,yxyx}-\chi^{(2)}_{q,zxzx}-\chi^{(2)}_{q,zyzy})\}$
$E^{PP}=\varepsilon_o \sin\theta' \cos\theta'\{[(\zeta^{(2)}_{q,xy}+\zeta^{(2)}_{q,yx})[\cos(4\phi)-1]$ $+4(\zeta^{(2)}_{q,xz}+\zeta^{(2)}_{q,zx}+\zeta^{(2)}_{q,yz}+\zeta^{(2)}_{q,zy})]\cos^2\theta'$ $+4(\chi^{(2)}_{q,xzxz}+\chi^{(2)}_{q,yzyz}-\chi^{(2)}_{q,zxzx}-\chi^{(2)}_{q,zyzy}-\zeta^{(2)}_{q,zx}-\zeta^{(2)}_{q,zy})\}$

radiation exhibits a ϕ-independent offset as well as a term proportional to $\cos(4\phi)$, while the *S*-detected radiation is proportional to $\sin(4\phi)$ with no offset. In either case the waveforms for the *P*- and *S*-polarized incident radiation are 180° out of phase. In the polarization calculation the amplitude associated with the 4ϕ term is the same for all four cases and is proportional to $\zeta^{(2)}_{q,xy}+\zeta^{(2)}_{q,yx}$ (where $\zeta^{(2)}_{q,ij}=\chi^{(2)}_{q,iiii}-\chi^{(2)}_{q,ijji}-\chi^{(2)}_{q,iijj}-\chi^{(2)}_{q,ijij}$), that describes the average anisotropy of $\chi^{(2)}_q$ in the *a*-*b* plane.[7] (We note that this amplitude is identically zero if the *a* and *b* directions are equivalent.) However, different Fresnel factors for the different polarizations result in somewhat different amplitudes measured for the radiated fields, a fact that is further complicated by the double refraction (neglected in the calculations presented in Table I) that occurs in this anisotropic material.[8]

As seen from Table I, there is a strong dependence on the angle of incidence such that the emission disappears at normal incidence ($\theta=0°$) for all polarizations, in agreement with experimental observations. The dependence of the peak-to-peak THz amplitude for E^{PP} on the angle θ' of the refracted wave for $YBa_2Cu_3O_7$ is plotted in Fig. 3(a) for $\phi=0°$ and 45°. From Table I the expected form of this data is $E^{PP}(\theta')=A\sin(2\theta')+B\sin(4\theta')$. The solid lines in Fig. 3(a) are fits of $E^{PP}(\theta')$ to the data. Moreover, in Fig. 3(b) we plot E^{PP} versus ϕ for $YBa_2Cu_3O_7$ at $\theta'=30°$ and 50°. The resultant fits to the data (solid lines) are $E^{PP}(\theta'=50°,\phi)=1.86\{\cos(4\phi)+2.7\}$ and $E^{PP}(\theta'=30°,\phi)=1.26\{\cos(4\phi)+2.6\}$. Therefore, the form of the two sets of data matches to within the uncertainty of the measurements, implying using Table I that $\chi^{(2)}_{q,xzxz}+\chi^{(2)}_{q,yzyz}-\chi^{(2)}_{q,zxzx}-\chi^{(2)}_{q,zyzy}-\zeta^{(2)}_{q,zx}-\zeta^{(2)}_{q,zy}=0$.

The absolute strength of the emission can be directly compared to bulk electric *dipole* χ^2 emission from material lacking inversion symmetry such as InP (excited above the band gap) by measuring E^{PS} from both semi-insulating InP and $YBa_2Cu_3O_7$, excited under the same conditions. By measuring *S*-detected emission we detect THz emission due solely to optical rectification, since we avoid detecting THz radiation from InP produced via carrier acceleration in the depletion field. In both cases the incident angle $\theta=50°$, while the azimuthal angle ϕ is set to maximize the THz output ($\phi=45°$ for InP and $\phi=22.5°$ for $YBa_2Cu_3O_7$). The waveforms have the same dispersion shape, but the amplitude of the InP emission is 12 times larger than the $YBa_2Cu_3O_7$ emission. This is an unexpectedly large value for electric quadrupole/magnetic dipole emission, since typically such a field is expected to be smaller than a dipole field

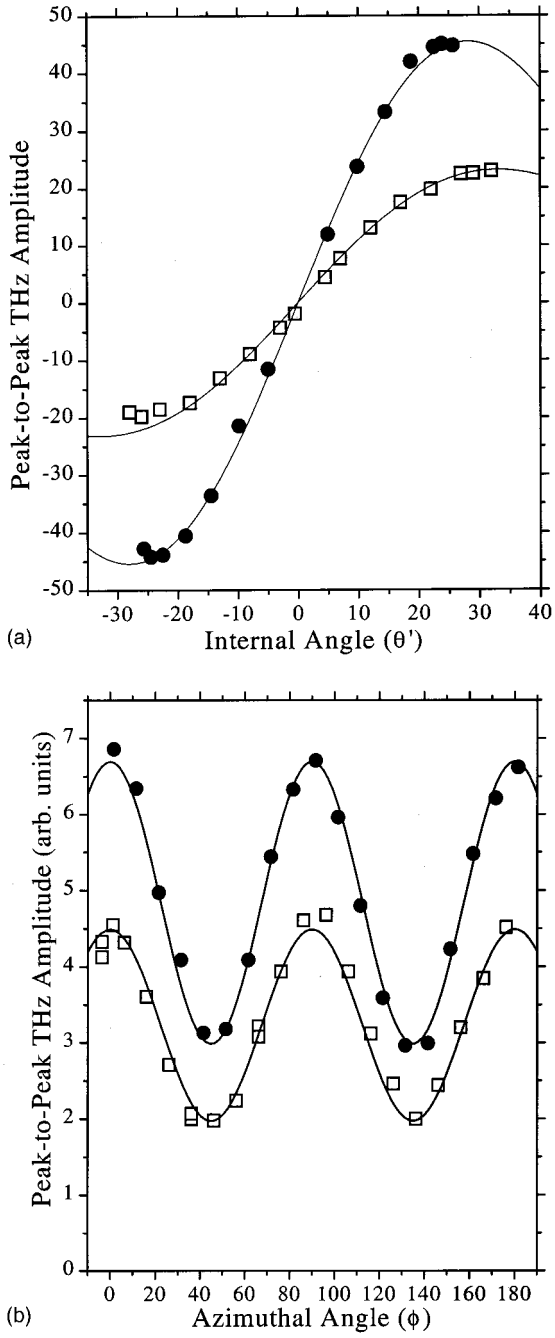

FIG. 3. (a) E^{PP} vs angle of refracted light, θ', for $YBa_2Cu_3O_7$ at $\phi=0°$ (circles) and $\phi=45°$ (squares). The uncertainty in the THz field amplitude is ±2. The solid line are fits of the data to the theoretically predicted form $E^{PP}(\theta')=A\sin(2\theta')+B\sin(4\theta')$. (b) E^{PP} vs ϕ for $YBa_2Cu_3O_7$ at $\theta'=30°$ (squares) and at $\theta'=50°$ (circles). The uncertainty in ϕ is ±2° and the uncertainty in the THz field amplitude is ±0.3. The resultant fits to the data (solid lines) are $E^{PP}(\theta'=50°,\phi)=1.86\{\cos(4\phi)+2.7\}$, and $E^{PP}(\theta'=30°,\phi)=1.26\{\cos(4\phi)+2.6\}$. The form of the two sets of data matches to within the uncertainty of the measurements.

TABLE II. Values of the material parameters used in the model to calculate the THz emission: the complex dielectric constant ε_i, the dc conductivity σ_i, and the relaxation time τ_i in each of the three crystallographic directions, $i=a$, b, and c. In the first column the values of these quantities for $YBa_2Cu_3O_7$ single crystals from Ref. 9 are given, while columns 2 and 3 list these quantities for $YBa_2Cu_3O_7$ and $YBa_2Cu_3O_{6.5}$ thin films, respectively, as determined by the fit of the model to our data.

	$YBa_2Cu_3O_7$ crystal (Ref. 9)	$YBa_2Cu_3O_7$ film	$YBa_2Cu_3O_{6.5}$ film
ε_a	$3.03+1.78i$	$3.04+1.84i$	$3.06+1.84i$
ε_b	$0.51+3.49i$	$0.52+3.45i$	$0.55+3.40i$
ε_c	$3.47+4.41i$	$3.47+4.41i$	$3.45+4.42i$
$\sigma_a,\sigma_b,\sigma_c$ (eV)	0.76, 1.65, 0.046	0.63, 1.70, 0.152	0.52, 1.73, 0.159
τ_a,τ_b,τ_c (eV^{-1})	2.00, 1.65, 1.00	2.03, 1.61, 1.00	2.06, 1.56, 1.01

by a factor of $ka=10^{-2}-10^{-3}$, where k is the visible wave vector and a is an atomic dimension. This large magnitude of electric quadrupole/magnetic dipole emission from $YBa_2Cu_3O_{7-\delta}$ probably results from the fact that the origin of the nonlinearity is free carriers in $YBa_2Cu_3O_{7-\delta}$ but bound or photoexcited carriers in InP. The fact that the amplitude of the emission from underdoped $YBa_2Cu_3O_{6.5}$ is roughly three times smaller than the emission from $YBa_2Cu_3O_7$ provides further evidence that free carriers are responsible for the nonlinearity which causes the emission, since this underdoped sample has fewer free carriers than $YBa_2Cu_3O_7$.

IV. MODELING

The observed THz emission can be explained in terms of the material properties of $YBa_2Cu_3O_{7-\delta}$. To first order, the electric field of the incoming light causes the free carriers in the film to oscillate at a frequency ω. There are two types of second-order responses: (a) The free carriers with a nonzero velocity $\mathbf{v}(t)=\mathbf{dx}(t)/dt$ from their first-order response interact with the magnetic field of light and experience an additional force $\mathbf{F}(t)$, proportional to $\mathbf{v}(t)\times\mathbf{B}(t)$, that leads to emission. (b) The carriers have a displacement $\mathbf{x}(t)$ from their first-order response. If $\mathbf{x}(t)$ is not orthogonal to the wave vector $\mathbf{k}$, there is a correction to the electric field experienced due to the $\exp(i\mathbf{k}\cdot\mathbf{x})$ spatial dependence of the electric field. Note that the material must be anisotropic for the displacement $\mathbf{x}$ to have a component parallel to $\mathbf{k}$. The magnetic dipole (a) and electric quadrupole (b) processes lead to emission at 2ω and $\omega\approx 0$. We observe the latter low-frequency process that leads to emission in the THz frequency range because of the width of the incoming optical pulse. The second-order force on a free carrier at frequency $\omega\approx 0$, due to both the electric quadrupole and magnetic dipole effects, is

$$F_\mu=-(e/2)\,\delta_{\mu\beta}\delta_{\gamma\nu}\,\mathrm{Im}[(x_\nu^1{}^*+x_\nu^2{}^*)(k_\beta^1E_\gamma^1+k_\beta^2E_\gamma^2)], \tag{2}$$

where e is the electron charge, E_γ^1 and E_γ^2 are the electric fields of the two transmitted (through double refraction) waves, k_β^1 and k_β^2 are the complex k vectors corresponding to E_γ^1 and E_γ^2, and x_ν^1 and x_ν^2 are the linear charge displacements due to the respective electric fields. ($x_\nu^i{}^*$ is the complex conjugate of x_ν^i, $\delta_{\mu\beta}$ is the identity matrix, and there is an implied sum over repeated indices.)

In this model the THz emission is calculated assuming a twinned crystal with orthorhombic symmetry. Twins with interchanged a and b axes, where b is the chain direction and a is the other in-plane direction, are assumed to occupy equal area on the sample. The dielectric tensor is complex, diagonal in the orthorhombic basis, and is specified at each frequency ω by three complex numbers. For a given incoming wave, we solve for the amplitude of the reflected and the two distinct transmitted waves, each with its own complex $\mathbf{k}$.[8] Because of the boundary conditions, the components of $\mathbf{k}$ in the a-b plane are real for the transmitted waves. The film is assumed to be much thicker than an optical depth.

We assume that the linear free carrier response (at dc and at ω) is described by the anisotropic Drude formula, $\sigma_\nu(\omega)=ne^2\tau_\nu/[m_\nu(1-i\omega\tau_\nu)]$, where ν indicates the a, b, or c direction. This form of the conductivity results in linear displacements x_ν^j:

$$x_\nu^j=ie\tau_\nu E_\nu^j/[\omega m_\nu(1-i\omega\tau_\nu)], \tag{3}$$

where $j=1$ and 2 for the two transmitted electric fields. Using Eqs. (2) and (3), we calculate the electric quadrupole and magnetic dipole THz current, including the cross terms between the two doubly refracted beams. Despite the simplicity of this model, 12 real numbers are required to specify the emission (the complex dielectric constant ε_i, the dc conductivity σ_i, and the relaxation time τ_i in each of the three crystallographic directions, $i=a,b,c$).

To compare the model with our data we use the experimentally determined parameters[9] for crystals of $YBa_2Cu_3O_7$ given in Table II, column 1, and calculate the resultant peak-to-peak THz field amplitude for E^{PP}, E^{SP}, E^{PS}, and E^{SS}, versus azimuthal angle ϕ. The calculated THz emission exhibits many of the same features as the emission data (Fig. 2) but is not in quantitative agreement with that data. To obtain quantitative agreement between our data and the model we vary the material parameters. Specifically, the χ^2 (the sum of the squared deviations) between our measurements of the peak-to-peak THz field amplitudes E^{PP}, E^{SP}, E^{PS}, and E^{SS} and the model is minimized by descending the gradient in the 12-dimensional parameter space starting with this initial set of parameters. The calculated THz emission using optimized parameters in our model is plotted in Fig. 4(a) for $YBa_2Cu_3O_7$, and Fig. 4(b) for $YBa_2Cu_3O_{6.5}$ (solid curves), along with the experimental data (points). The values of the material parameters resulting from this optimization are given in Table II along with the values from Reference 9

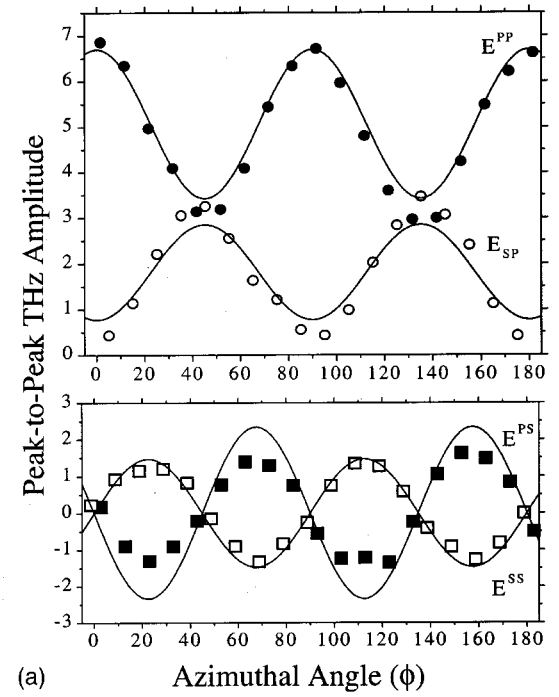

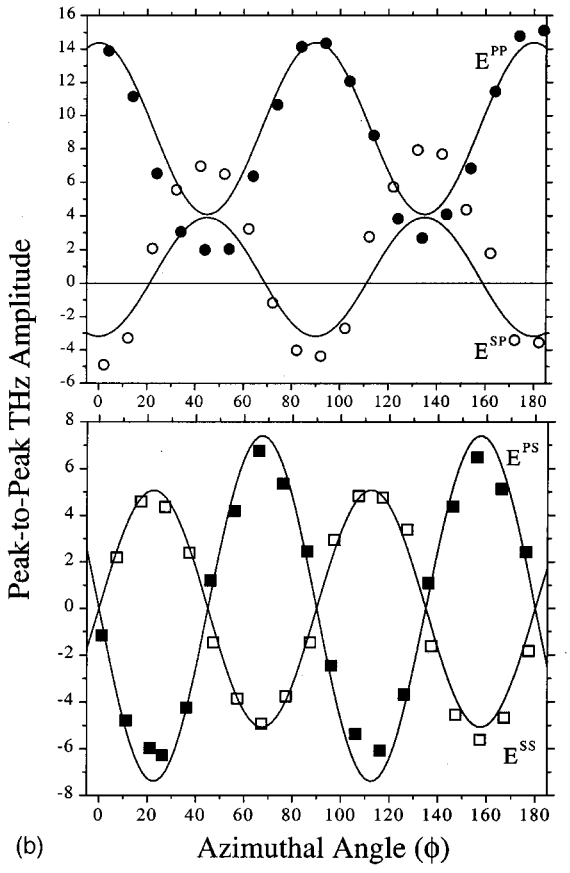

FIG. 4. Calculated peak-to-peak THz emission using optimized parameters in our model (solid lines) and measured peak-to peak THz emission (points) for $YBa_2Cu_3O_7$ (a) and $YBa_2Cu_3O_{6.5}$ (b) vs azimuthal angle, ϕ. For (a), the uncertainty in ϕ is $\pm 2°$, and the uncertainty in the THz field amplitude is ± 0.3. For (b), the uncertainty in ϕ is $\pm 2°$, and the uncertainty in the THz field amplitude is ± 0.6.

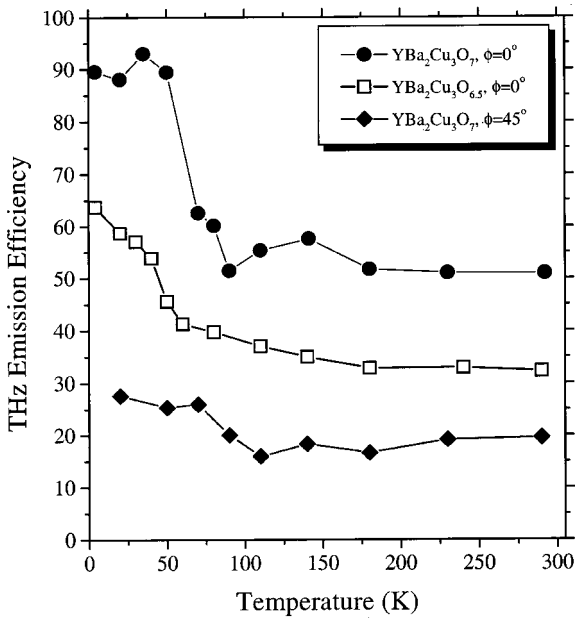

FIG. 5. Emission efficiency vs temperature for a 60-nm-thick $YBa_2Cu_3O_7$ film ($T_c = 85$ K), excited at $\theta = 50°$, $\phi = 0°$ (solid circles, fractional uncertainty $= \pm 5\%$), and $\phi = 45°$ (solid diamonds, the fractional uncertainty is $\pm 15\%$), and for a 300-nm-thick $YBa_2Cu_3O_{6.5}$ film ($T_c = 55$ K), excited at $\theta = 50°$, $\phi = 0°$ (open squares; the fractional uncertainty is $\pm 7\%$). The emission has been corrected for the temperature-dependent THz absorption.

measured on untwinned, single crystal $YBa_2Cu_3O_7$ samples using linear spectroscopic techniques. The fit shown in Fig. 4(a), using the parameters given in the second column of Table II is 24 times better (as measured by χ^2) than the fit obtained with the single crystal parameters of Ref. 9 (first column of Table II). The fit in Fig. 4(b) is 16 times better. The difference between the calculations and experiment may be due to the inadequacy of the assumption of a Drude conductivity, especially at 1.5 eV.

A comparison of the measured THz emission for $YBa_2Cu_3O_7$ (points) with the calculated emission (solid curves) in Fig. 4(a) yields good agreement except for the amplitude of E^{PS}, while a comparison of the measurements for $YBa_2Cu_3O_{6.5}$ with the calculations [Fig. 4(b)] shows better agreement for the *S*-detected emission than for the *P*-detected emission. The only parameters that changed significantly during this optimization were the dc conductivities σ_i; other parameters (complex dielectric constants ε_i at 1.5 eV, and the relaxation times τ_i) all changed by less than 10%. Significantly higher values for the *c*-axis conductivity are found, $\sigma_c = 0.152$ eV for $YBa_2Cu_3O_7$ and $\sigma_c = 0.159$ eV for $YBa_2Cu_3O_{6.5}$, as compared to the value of $\sigma_c = 0.046$ eV from Ref. 9. A higher value for the ratio of the chain to plane conductivities σ_b/σ_a results from this data with a ratio of 2.7 for $YBa_2Cu_3O_7$ and 3.3 for $YBa_2Cu_3O_{6.5}$, as compared to 2.2 for $YBa_2Cu_3O_7$ from Ref. 9. This apparent discrepancy may be caused by the difference in conductivities between untwinned single crystals and twinned thin films. We further note that the anisotropic conductivity cannot be determined in twinned samples using linear transport measurements.

V. TEMPERATURE-DEPENDENT EMISSION

The temperature dependence of the emission (E^{PP}) is characterized over the range of temperatures T, $4\,K<T<300\,K$, where the films change from superconductors to correlated metals. Since the absorption of THz radiation increases enormously below the superconducting transition temperature, we measure THz transmission at each temperature, and use these data to calculate a THz emission efficiency that is independent of the absorption. In Fig. 5 we plot the temperature dependence of this emission efficiency for $YBa_2Cu_3O_7$ at $\phi=0°$ and 45° (maximum and minimum emission angles), as well as for $YBa_2Cu_3O_{6.5}$ at $\phi=0°$. For $YBa_2Cu_3O_7$ the emission exhibits the same behavior for both values of ϕ: It is roughly constant between 300 K and the superconducting transition temperature $T_C=85\,K$, where it abruptly increases, leveling off at low temperature to a value 65% higher than that measured for the normal state. The $YBa_2Cu_3O_7$ data in Fig. 5 fit reasonably well to a two-fluid model using $T_C=85\,K$, and yield a ratio for superfluid to normal emission efficiency of 1.65.

A simple two-fluid model describes the temperature dependence of the emission from $YBa_2Cu_3O_{6.5}$ less well. The temperature dependence of emission from $YBa_2Cu_3O_{6.5}$ exhibits a similar but slightly different behavior than $YBa_2Cu_3O_7$ in that the emission is constant from $T=300$ to 180 K, then increases slowly but monotonically down to $T_C=55\,K$, where it abruptly increases, peaking at low temperature to a value twice as large as at $T=300\,K$. Such behavior is consistent with the opening of a spin gap in the underdoped material at 180 K. If the normal carriers couple strongly to spin fluctuations in these materials, then the opening of the spin gap at a temperature T^* should be accompanied by an increase in the scattering time, giving rise to an enhancement in the real conductivity below T^*.[10] Another possible explanation is that above T_C, the superconducting phase correlations are finite in space and time.[11,12] An enhancement of the conductivity for temperatures T such that $T_C<T<T^*$ was observed in both dc and THz conductivity measurements in underdoped cuprates.[13,14] Such an increase in the real conductivity for $T_C<T<T^*=180\,K$ in $YBa_2Cu_3O_{6.5}$ would result in an increase in the THz emission over that temperature range, as observed in Fig. 5.

VI. CONCLUSIONS

In conclusion, we report the observation of THz emission from unbiased thin films excited by 1.5-eV, 150-fs pulses. This emission is characterized for optimally doped, $\delta=0$, and underdoped, $\delta=0.5$ films, over a range of temperatures T, $4\,K<T<300\,K$, where the films change from superconductors to correlated metals. We demonstrate that this emission is generated by optical rectification due to the bulk electric quadrupole and magnetic dipole source terms, comprising what we believe to be the first observation of such a source term in THz emission. A model of this emission, assuming that the nonlinearity results from transport of carriers with different masses and relaxation times in the three crystallographic direction, is consistent with the data. A fit of the data to this model yields values for the anisotropic masses and relaxation times in $YBa_2Cu_3O_{7-\delta}$ thin films.

ACKNOWLEDGEMENT

We acknowledge several helpful discussions with T. F. Heinz. This research was supported through the Los Alamos Directed Research and Development Program of the U.S. Department of Energy.

*FAX: (505) 665-7652. Email: ttaylor@lanl.gov

[1] S. L. Chuang, S. Schmitt-Rink, B. I. Greene, P. N. Saeta, and A. F. J. Levi, Phys. Rev. Lett. **68**, 102 (1992).

[2] X.-C. Zhang, B. B. Hu, J. T. Darrow, and D. H. Auston, Appl. Phys. Lett. **56**, 1011 (1990).

[3] H. G. Roskos, M. C. Nuss, J. Shah, K. Leo, D. A. B. Miller, A. M. Fox, S. Schmitt-Rink, and K. Kohler, Phys. Rev. Lett. **68**, 2216 (1992).

[4] T. Dekorsy, H. Auer, C. Waschke, H. J. Bakker, H. G. Roskos, H. Kurz, V. Wagner, and P. Grosse, Phys. Rev. Lett. **74**, 738 (1995).

[5] M. Tonouchi, M. Tani, Z. Wang, K. Sakai, S. Tomozawa, M. Hangyo, Y. Murakami, and S. Nakashima, Jpn. J. Appl. Phys. **35**, 2524 (1996).

[6] M. Tonouchi, M. Tani, Z. Wang, K. Sakai, N. Wada, and M. Hangyo, Jpn. J. Appl. Phys., Part 2 **36**, L93 (1997).

[7] T. F. Heinz, in *Nonlinear Surface Electromagnetic Phenomena*, edited by H. E. Ponath and G. I. Stegeman (North-Holland, Amsterdam, 1991), p. 369.

[8] L. D. Landau and E. M. Lifshiftz, *Electrodynamics of Continuous Media* (Elsevier, Oxford, 1984), p. 340.

[9] Tsu-Wei Nee, J. Appl. Phys. **71**, 6002 (1992).

[10] T. Ito, K. Takenaka, and S. Uchida, Phys. Rev. Lett. **70**, 3995 (1993).

[11] J. Corson, R. Mallozzi, J. Orenstein, J. N. Eckstein, and I. Bozovic, Nature (London) **398**, 221 (1999).

[12] V. J. Emery and S. A. Kivelson, Nature (London) **374**, 434 (1995).

[13] R. Buhleier, S. D. Brorson, I. E. Trofimov, J. O. White, H.-U. Habermeier, and J. Kuhl, Phys. Rev. B **50**, 9672 (1994).

[14] C. Ludwig, Q. Jian, J. Kuhl, and J. Zegenhagen, Physica C **269**, 249 (1996).